

## Polyacrylonitrile template-assisted formation of $\text{LiMn}_2\text{O}_4$ nanoparticles for lithium-ion batteries

Bon-Ryul Koo<sup>a</sup> and Hyo-Jin Ahn<sup>a,b,\*</sup>

<sup>a</sup>Program of Materials Science & Engineering, Convergence Institute of Biomedical Engineering and Biomaterials, Seoul National University of Science and Technology, Seoul 139-743, Korea

<sup>b</sup>Department of Materials Science and Engineering, Seoul National University of Science and Technology, Seoul 139-743, Korea

In this study,  $\text{LiMn}_2\text{O}_4$  (LMO) nanoparticles were fabricated using polyacrylonitrile (PAN) templates and the annealing process. In order to optimize their electrochemical performance for LIBs, we adjusted the annealing temperatures to 600, 700, 800, and 900 °C. For comparison, the LMO particles were prepared using the solid-state reaction method. Interestingly, due to the limited grain growth and aggregation of the LMO by the PAN templates, the samples prepared by the PAN templates annealed at 700 °C revealed the nanoparticles below ~150 nm in size. As compared to other samples, the LMO nanoparticles prepared at 700 °C showed a superb specific discharge capacity of ~103.6 mAh/g at 100 cycles (capacity retention of ~82.7%) and a good high-rate performance (~81.8 mAh/g at 5 C). These outstanding electrochemical performances are due to the shortened diffusion distance of  $\text{Li}^+$  by the LMO nanoparticles thanks to the PAN templates and the improved electroactive sites by the correct stoichiometric LMO phases without impurities at the optimum annealing temperature. Thus, these results indicate that the LMO nanoparticles formed via the PAN templates annealed at 700 °C could be used as promising cathode materials for high-performance LIBs.

**Key words:** Lithium-ion batteries, Cathodes,  $\text{LiMn}_2\text{O}_4$ , Nanoparticles, Polyacrylonitrile templates.

### Introduction

Due to their high energy density, high voltage, and environmental friendliness, lithium-ion batteries (LIBs) have been promisingly developed into the main power sources for various applications, such as portable power tools, hybrid electric vehicles (EVs), and medical equipment [1-3]. A conventional LIB consists of four main components, including the cathode, the anode, the electrolyte, and the separator. Among these components, the electrode materials such as cathode and anode are important factors that directly determine the electrochemical performance of LIBs, including the energy density, potential window, cycling stability, and rate performance [4]. In particular, the cathode materials are characterized by a high cost and a relatively poor electrochemical performance, as compared to the anode materials, which is one of main challenges to expand the use of LIBs in future electronic applications (EVs and plug-in-hybrid) requiring high energy and power density [5, 6]. Thus, much effort has been invested into the development of various cathode materials with outstanding performances in the LIBs. Among the cathode materials reported until now,  $\text{LiMn}_2\text{O}_4$  (LMO) materials, which exhibit the spinal

structure with three-dimensional lithium diffusion paths and have the advantages of high potential, good safety, low toxicity, and abundant Mn elements, have attracted much attention as potential candidate for replacing  $\text{LiCoO}_2$  materials used in commercial LIBs [4, 7, 8]. Nevertheless, due to their relative low diffusion coefficient of  $\text{Li}^+$  ( $10^{-9}$ - $10^{-11}$   $\text{cm}^2 \text{ s}^{-1}$ ), poor cycling performance or poor rate performance are frequently observed in LIBs using the LMO electrode [4]. An effective strategy to solve these problems is to decrease the particle size and form the nanopores at the LMO electrode, which can enhance the diffusion rate of  $\text{Li}^+$  due to the shortened transport distance of  $\text{Li}^+$  at the particles and the increased electroactive sites between the electrode material and the electrolyte [8]. It is well-known that LMO is prepared by a conventional solid-state reaction at the annealing temperature of 700-900 °C [7, 8]. However, this method lends many weaknesses to the products, including irregular morphology, inhomogeneity, large particle size, impurity phases, and broad distribution of particle size, resulting to poor electrochemical performances for LIBs [7, 8]. Recently, several synthetic processes, such as sol-gel and hydrothermal methods, have been proposed to obtain the LMO nanoparticles with a homogeneous size distribution [4, 9, 10]. However, there are no reports on the development of the LMO nanoparticles through polyacrylonitrile template-assisted synthetic processes.

In the present study, we prepared the LMO nanoparticles

\*Corresponding author:  
Tel : +82-2-970-6622  
Fax: +82-2-973-6657  
E-mail: hjahn@seoultech.ac.kr

via the PAN templates prepared by the electrospinning technique, which has the advantages of low cost, simple set-up, large-scale productivity [11]. To optimize the electrochemical performances of LIBs, four different annealing temperatures were used: 600, 700, 800, and 900 °C.

## Experimental Details

The LMO nanoparticles were fabricated using the PAN templates with the different annealing temperatures. For the preparation of the PAN templates using electrospinning, 10 wt% PAN ( $M_w = 150,000$  g/mol, Aldrich) was dissolved in *N,N*-dimethylformamide (DMF, 99.8%, Aldrich). Then, the resulting solution was transferred into a syringe equipped with a 23-gauge needle. The voltage between the needle and the collector was maintained at 13 kV under the distance of 15 cm and the feeding rate of 0.03 ml/hr, resulting in the formation of the PAN templates [12]. Subsequently, the sol treatment of the PAN templates was performed by immersing the prepared PAN into the sol solution including lithium acetate dihydrate ( $\text{CH}_3\text{COOLi}\cdot 2\text{H}_2\text{O}$ , Aldrich) and manganese (II) acetate tetrahydrate ( $(\text{CH}_3\text{COO})_2\text{Mn}\cdot 4\text{H}_2\text{O}$ , Aldrich) in de-ionized (DI) water. The weight ratio of the Mn precursor to the solvent was applied to 10 wt% and the molar ratio of Mn/Li was fixed at 2 to obtain stoichiometric LMO phases [13]. After drying at 80 °C, in order to optimize their electrochemical performances of LIBs, the sol-treated PAN templates were annealed at different temperatures (600, 700, 800, and 900 °C). Therefore, we prepared four different types of the LMO nanoparticles: nano-LMO/600, nano-LMO/700, nano-LMO/800, and nano-LMO/900. For comparison, the LMO particles were also prepared using the solid-state reaction method at the annealing temperature of 700 °C (referred to herein as S-LMO/700) [14].

The measurements of the crystal structure and chemical binding state of the samples were made from X-ray diffraction (XRD, Rigaku D/Max-2500 diffractometer using  $\text{Cu K}_\alpha$  radiation) and X-ray photoelectron spectroscopy (XPS, ESCALAB 250 equipped with an Al  $\text{K}_\alpha$  X-ray source), respectively. The morphology and structure were observed using field-emission scanning electron microscopy (FESEM, Hitachi S-4800) and transmission electron microscopy (MULTI/TEM; Tecnai G<sub>2</sub>, KBSI Gwangju Center).

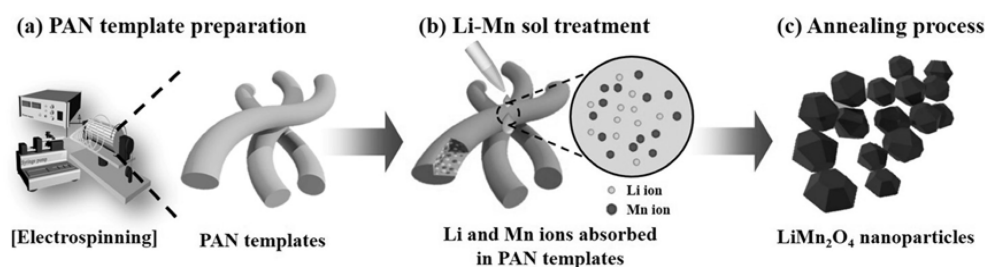
The evaluation of electrochemical performances on the samples was performed using coin cells (CR2032) composed of the prepared LMO samples as the cathode, Li metal foil as the anode, a polypropylene membrane as the separator, and 1.0 M  $\text{LiPF}_6$  solution in a mixture of ethylene carbonate (EC) and diethyl carbonate (DEC) (volume ratio of 1:1) as the electrolyte. To fabricate the cathode electrode, slurries prepared by mixing the active materials (80 wt%),

Ketjen black (10 wt%), and poly(vinylidene fluoride) (10 wt%) (Alfa Aesar) into an *N*-methyl-2-pyrrolidinone solvent were coated onto an Al foil using a doctor blade. Then, the resultant electrodes were dried at 100 °C for 12 hrs in an air oven. All assembly of the Li-ion cells was performed in a glovebox filled by a high purity argon. The charge/discharge measurements within a potential range of 3.0–4.5 V versus  $\text{Li/Li}^+$  were carried out using a battery cycler system (WonAtech Corp., WMPG 3000) in an incubator at 25 °C. The stability and rate performance of the samples were measured using the above-obtained test equipment at 1 C and the varied current rates of 0.5, 1.0, 3.0, 5.0, and 1.0 C. The electrochemical impedance spectroscopy (EIS) measurements were performed using fresh cells to investigate their electrochemical kinetics with an AC signal of 5 mV in the frequency range from 100 kHz to 10 mHz.

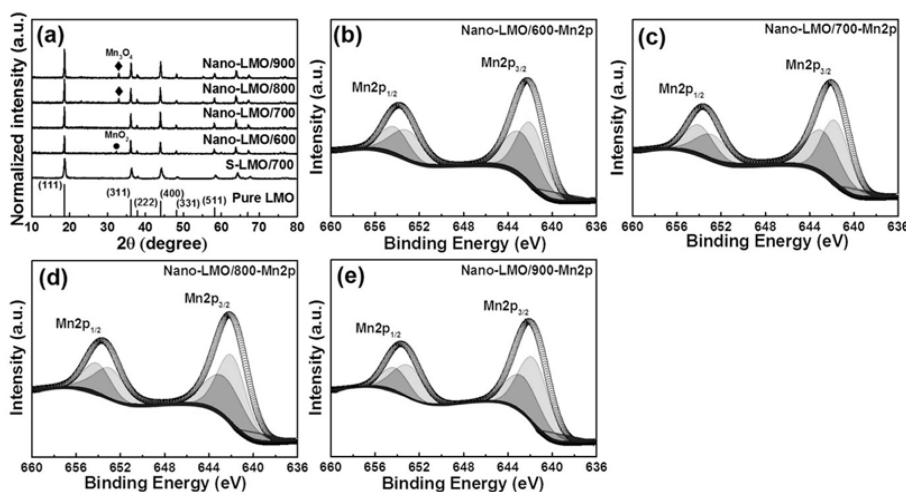
## Results and Discussion

Fig. 1 is a schematic illustration of the ideal process for fabricating the LMO nanoparticles using the PAN templates. First, the PAN templates were prepared by electrospinning (Fig. 1(a)). To obtain the LMO nanoparticles, the prepared PAN templates were immersed in the sol solution with Li and Mn ions in DI water (Fig. 1(b)). According to a previous report, the PAN is insoluble due to its hydrophobicity [12]. Thus, in our study, one-dimensional nanostructure of the PAN templates remained morphologically unchanged after the sol treatment with DI water. Also, during the sol treatment, due to the hydrophilic property of amidoxime group in the PAN, the Li and Mn ions were absorbed to the PAN [15]. After the annealing process (Fig. 1(c)), the sol-treated PAN templates underwent the grain growth of the LMO phases in PAN and then PANs were removed by its combustion. According to the results of previous studies, the LMOs generally generate the aggregation by their grain growth as the annealing temperature increases, which can lead to the formation of submicron LMO products with a broad distribution of particle size and an irregular morphology relative to the poor electrochemical performance [7, 8]. Therefore, the use of the PAN templates could affect the formation of the LMO nanoparticles with regular particle size and morphology because the PAN templates can assist in preventing the irregular growth of the LMO grain and the aggregation of the LMO nanoparticles [16].

Fig. 2(a) shows the XRD patterns for defining the crystal structure of the samples. In all samples, the characteristic diffraction peaks are equally emitted at 18.6°, 36.1°, and 43.9°, corresponding to (111), (311), and (400) planes of the spinal LMO with space group of  $\text{Fd-3m}$  (JCPDS no. 35-0782), respectively. The observed peak intensities are gradually enhanced with an increase of the annealing temperature, which is



**Fig. 1.** Schematic representation for synthesizing the LMO nanoparticles through sol treatment of the PAN templates.



**Fig. 2.** (a) XRD patterns obtained from all samples and XPS core-level spectra of (b) nano-LMO/600, (c) nano-LMO/700, (d) nano-LMO/800, and (e) nano-LMO/900.

related to the formation of the LMO phase with a large particle size. However, nano-LMO/600 reveals a weak extra peak ( $32.9^\circ$ ) corresponding to (222) plane of cubic  $\text{Mn}_2\text{O}_3$  (JCPDS no. 71-0636). This phase is obtained due to the insufficient annealing temperature [17]. In addition, at an annealing temperature over  $800^\circ\text{C}$ , there is another peak emitted at  $33.5^\circ$ , which is consistent with (320) plane of orthorhombic  $\text{Mn}_3\text{O}_4$  (JCPDS no. 86-2337) formed due to the partial decomposition of LMO [18]. These results reveal that the annealing process at  $700^\circ\text{C}$  (nano-LMO/700) leads to a successful formation of the LMO nanoparticles without  $\text{Mn}_2\text{O}_3$  or  $\text{Mn}_3\text{O}_4$  phases. In order to further characterize the chemical bonding states, we performed the XPS measurements (see Figs. 2(b-e)). The Mn  $2p_{3/2}$  and Mn  $2p_{1/2}$  XPS core-level spectra reveal two major peaks: one at  $\sim 641.5$  eV for Mn  $2p_{3/2}$  and  $\sim 652.7$  eV for Mn  $2p_{1/2}$  corresponding to binding energy of  $\text{Mn}^{3+}$  and the other at  $\sim 642.7$  eV for Mn  $2p_{3/2}$  and  $\sim 653.9$  eV for Mn  $2p_{1/2}$  corresponding to  $\text{Mn}^{4+}$  [19, 20]. Interestingly, for nano-LMO/700 (Fig. 2(c)), the area ratio of  $\text{Mn}^{3+}$  versus  $\text{Mn}^{4+}$  is 1 : 1, which is a good match with the theoretical stoichiometric value of the spinal LMO phase [21]. On the other hand, the increased area ratios of  $\text{Mn}^{3+}/\text{Mn}^{4+}$  are observed in the XPS core-level spectra of the other samples, which is due to the formation of  $\text{Mn}_2\text{O}_3$  phase for nano-LMO/

600 (Fig. 2(b)) and  $\text{Mn}_3\text{O}_4$  phase for nano-LMO/800 (Fig. 2(d)) and nano-LMO/900 (Fig. 2(e)), corresponding to the equivalent results of the obtained XRD patterns (Fig. 2(a)) [22]. Therefore, the XRD and XPS results suggest that nano-LMO/700 has the spinal LMO phase without formation of the  $\text{Mn}_2\text{O}_3$  or  $\text{Mn}_3\text{O}_4$  phases.

Fig. 3 shows the FESEM images of S-LMO/700, nano-LMO/600, nano-LMO/700, nano-LMO/800, and nano-LMO/900. As shown in Fig. 3(a), S-LMO/700 prepared by the solid-state reaction method has non-uniform aggregates of submicron particles size [14]. On the other hand, all samples obtained from the PAN templates (see Figs. 3(b-e)) present a semi-spherical morphology with well-defined crystal faces and, due to the promoted grain growth (115.3-131.4 nm for nano-LMO/600, 126.6-143.7 nm for nano-LMO/700, 241.6-280.1 nm for nano-LMO/800, and 470.3-1,324.0 nm for nano-LMO/900), their sizes are gradually improved with an increase of the annealing temperature from  $600^\circ\text{C}$  to  $900^\circ\text{C}$  [7]. Thus, at the annealing temperature of  $700^\circ\text{C}$ , it can lead to the formation of uniformly distributed nanoparticles, which is due to the existence of the PAN templates that can limit the grain growth and aggregation of the LMO nanoparticles. Thus, due to the enhanced contact area with electrolyte and shorted diffusion length of lithium ions during discharge and charge processes, the formation of the LMO nanoparticles

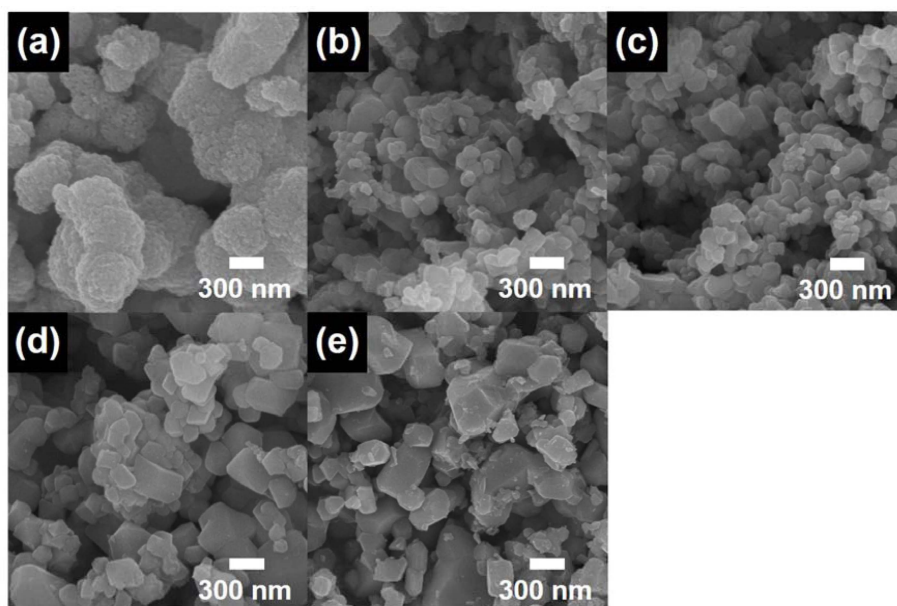


**Fig. 3.** SEM images of (a) S-LMO/700, (b) nano-LMO/600, (c) nano-LMO/700, (d) nano-LMO/800, and (e) nano-LMO/900.

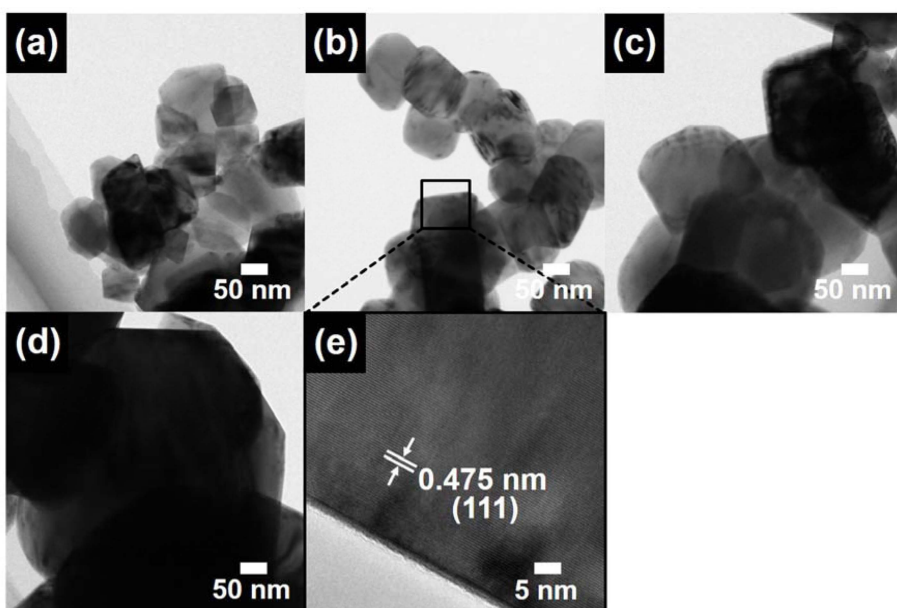


**Fig. 4.** TEM images of (a) nano-LMO/600, (b) nano-LMO/700, (c) nano-LMO/800, and (d) nano-LMO/900 and (e) high-resolution TEM image obtained from nano-LMO/700.

through the PAN templates could be useful in the improvement of cycleability and rate-performance for LIBs [4, 8].

To further examine the nanostructures of the LMO nanoparticles fabricated using the PAN templates, we performed the TEM measurement. As shown in Fig. 4, the LMO nanoparticles have a semi-spherical shape without aggregation. Furthermore, the average particle sizes were observed to be 120.6–130.8 nm for nano-LMO/600, 127.4–143.4 nm for nano-LMO/700, 242.2–264.6 nm for nano-LMO/800, and 533.8–889.0 nm for nano-LMO/900, indicating an increase in the particle size as a result of the increased annealing temperature.

Interestingly, the HRTEM result of nano-LMO/700 (Fig. 4(e)) evidently shows clear lattice fringes with the spacing of 0.475 nm corresponding to the (111) diffraction planes of the spinel LMO crystal, revealing a high crystallinity of the LMO nanoparticles [4, 23]. Therefore, these results support the successful formation of the high-crystallized LMO nanoparticles via the PAN templates.

Fig. 5(a) shows the galvanostatic charge-discharge profiles obtained from nano-LMO/600, nano-LMO/700, nano-LMO/800, and nano-LMO/900 electrodes at the current rate of 1 C between 3.0 and 4.5 V (vs. Li/Li<sup>+</sup>). There are two voltage plateaus at 4.00/3.90 V for

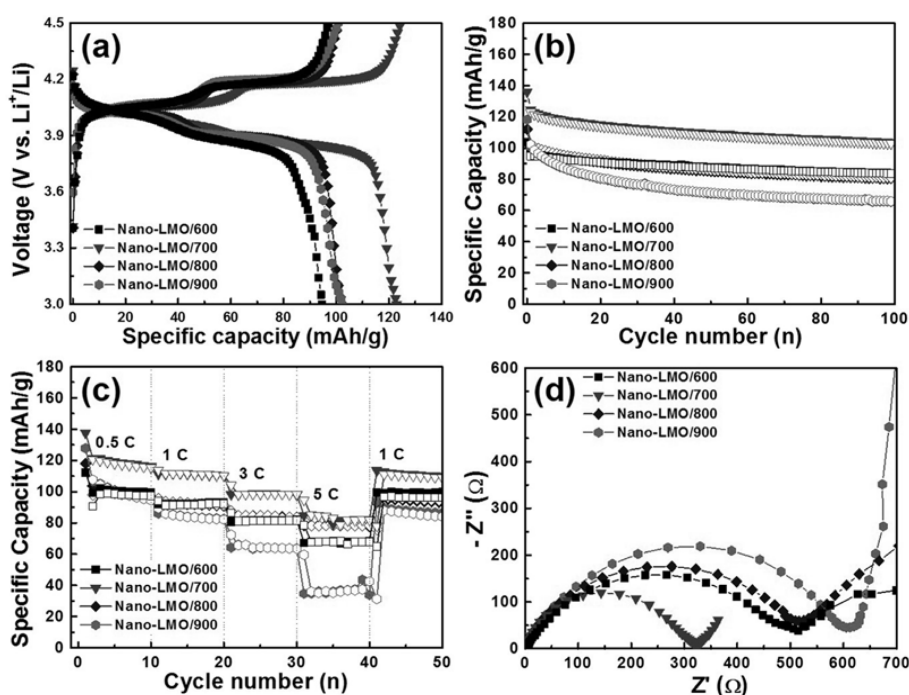


**Fig. 5.** (a) Galvanostatic charge-discharge profiles of the LIBs cells fabricated with the nano-LMO/600, nano-LMO/700, nano-LMO/800, and nano-LMO/900 electrodes measured at current rate of 1 C in potential range from 3.0 to 4.5 V, (b) cycling stabilities at a current rate of 1 C up to 100 cycles. (c) rate performances measured at current rate of 0.5 C to 1, 3, 5, and 1 C, and (d) Nyquist plots in the frequency range between 100 kHz and 100 mHz before the charge-discharge tests.

**Table 1.** Discharge capacity comparison of the LIBs fabricated with the LMO nanoparticles electrodes using synthetic methods reported previously.

Processes	Current rate (C)	Discharge capacity (mAh/g)	References
Cellulose-assisted combustion method	~ 1.0	~ 100.0	[4]
Resorcinol-formaldehyde method 1	~ 1.0	~ 80.0	[8]
Resorcinol-formaldehyde method 2	~ 0.5	~ 110.0	[13]
Hydrothermal method 1	~ 0.5	~ 111.0	[26]
Hydrothermal method 2	~ 0.2	~ 102.0	[27]
Solid state method	~ 0.2	~ 73.5	[28]
Polyethyleneglycol-assisted method	~ 1.0	~ 100.0	[29]
PAN template-assisted method	~ 1.0	~ 103.6	This work

discharging and 4.06/4.18 V for charging. This observation is associated with the characteristic deintercalation and intercalation reaction of  $\text{Li}^+$  in 8a tetrahedra sites of the LMO phase [24]. As a result, the initial specific discharge capacities are observed to be ~ 94.6 mAh/g for the nano-LMO/600 electrodes, ~ 122.9 mAh/g for the nano-LMO/700 electrodes, ~ 102.1 mAh/g for the nano-LMO/800 electrodes, and ~ 102.3 mAh/g for the nano-LMO/900 electrodes. In particular, the nano-LMO/700 electrodes exhibit the highest initial specific capacities (~ 83.0% of the theoretical capacity of LMO (148 mAh/g)) among the others, which is induced due to the formation of nanoparticles with the correct stoichiometric LMO phases. Furthermore, due to presence of the  $\text{Mn}_2\text{O}_3$  phases relative to non-electroactive sites, the nano-LMO/600 electrodes present relatively low initial specific capacities. The observed

low initial specific capacities of the nano-LMO/800 and nano-LMO/900 electrodes are related to the increased particle sizes and existence of  $\text{Mn}_3\text{O}_4$  phases related to non-electroactive sites caused by a high annealing temperature. Fig. 5(b) shows the cycling stability of the specific capacities on the electrodes at the current rate of 1 C. At 100 cycle, the capacity retention is observed at ~ 86.3, ~ 82.7, 80.5, and 64.3% for the nano-LMO/600, nano-LMO/700, nano-LMO/800, and nano-LMO/900 electrodes, respectively, indicating a gradually enhanced capacity retention with a decrease of annealing temperature of the LMO nanoparticles prepared by the PAN templates. This performance variation is mainly ascribed to the shortened diffusion pathway of  $\text{Li}^+$  relative to the decreased particle size of the LMO nanoparticles [25]. Of note, the nano-LMO/700 electrodes reveal an impressive cycling stability

with a high specific discharge capacity of  $\sim 103.6$  mAh/g after 100 cycles, which, compared to previous reports [4, 8, 13, 26-29], corresponds to the superb performance of the LMO nanoparticles, despite the measurement at the current rate of 1 C (see Table 1). In addition, we investigated their rate performance by varying the current rate from 0.5 C to 1, 3, 5, and 1 C (see Fig. 5(c)). For the nano-LMO/700 electrodes, the reversible discharge capacities of  $\sim 120.6$ ,  $\sim 115.4$ ,  $\sim 110.9$ ,  $\sim 98.3$ , and  $\sim 81.8$  mAh/g were reached at 0.5, 1, 3, and 5 C, respectively. Furthermore, their reversible discharge capacities were recovered at  $\sim 109.0$  mAh/g when the current rate reverted to 1 C. This remarkable result can be ascribed to the easier lithium behavior in the LMO nanoparticles by the shorted diffusion distance of  $\text{Li}^+$  and improved electroactive sites resulting from the formation of the correct stoichiometric LMO phases. In order to determine the transfer behavior of  $\text{Li}^+$ , the measurement of EIS was performed using fresh cells. Fig. 5(d) shows the Nyquist plots, with a semicircle in the high-frequency zone relative to a charge transfer at the cathode-electrolyte interface and a straight line (Warburg impedance) in the low-frequency zone reflecting the solid state diffusion of  $\text{Li}^+$  in the cathode [19]. As can be seen in the Nyquist plots, the nano-LMO/700 electrodes possess smaller semicircle than the other electrodes, which is indicative of the increased charge transfer at the surface of the cathode to improve the Li intercalation-deintercalation process for LIBs [30]. However, as compared to the nano-LMO/700 electrodes, the other electrodes have a relatively large semicircle because of the existence of the  $\text{Mn}_2\text{O}_3$  phase, despite the formation of nanoparticles for nano-LMO/600 electrodes and the increased particle size as well as the formation of  $\text{Mn}_3\text{O}_4$  phases for the nano-LMO/800 and nano-LMO/900 electrodes. Therefore, the LMO nanoparticles fabricated via the PAN templates (nano-LMO/700 electrodes) are successfully proven to have superb electrochemical performances for LIBs, which can be attributed to the combined effect of the shorted diffusion pathway of  $\text{Li}^+$  in the LMO nanoparticles allowing the improvement of capacity retention and high-rate performance, and the enhanced electroactive sites of the correct stoichiometric LMO phases enhancing the specific discharge capacity. These results suggest that the LMO nanoparticles prepared by the PAN templates are promising candidates for being used as cathode materials in LIBs.

## Conclusions

In the present study, we successfully fabricated the LMO nanoparticles through the PAN templates as a novel synthetic route. This method resulted to the formation of regular LMO nanoparticles below  $\sim 150$  nm due to the limited grain growth and aggregation by the presence of the PAN templates,

while a solid-state reaction method formed the non-uniform aggregates of submicron particle size. The formation of the LMO nanoparticles ensured short diffusion paths of  $\text{Li}^+$  in the electrodes and an enhancement of electroactive sites for the deintercalation and intercalation reactions of  $\text{Li}^+$ . Thus, by optimized the annealing temperature, the electrochemical results demonstrate that, as compared to other electrodes, the electrodes fabricated with the LMO nanoparticles at  $700^\circ\text{C}$  (nano-LMO/700 electrodes) have a good specific discharge capacity ( $\sim 103.6$  mAh/g) after 100 cycles (capacity retention of  $\sim 82.7\%$ ), as well as an outstanding high-rate performance ( $\sim 81.8$  mAh/g at 5 C). These superb electrochemical performances are attributed to the synergistic effect of the shorted diffusion distance of  $\text{Li}^+$  in the LMO nanoparticles formed by the PAN templates and the enhanced electroactive sites of the correct stoichiometric LMO phases without the  $\text{Mn}_2\text{O}_3$  or  $\text{Mn}_3\text{O}_4$  phases. Therefore, we demonstrated that the LMO nanoparticles formed via the PAN templates are promising candidates for being used as cathode material in LIBs.

## Acknowledgments

This work was supported by the Industrial Fundamental Technology Development Program (1005 2745, Development of nano-sized (100 nm) manganese ceramic material for high voltage pseudo-capacitor) funded by the Ministry of Trade, Industry and Energy (MOTIE) of Korea.

## References

1. T. Waket, T. Sarakonsri, K. E. Aifantis, and S. A. Hackney, *J. Ceram. Process. Res.* 17 (2016) 73-79.
2. G.-H. An and H.-J. Ahn, *J. Power Sources* 272 (2014) 828-836.
3. K. W. Kang, Y. U. Jeong, and Y. J. Lee, *J. Ceram. Process. Res.* 17 (2016) 54-58.
4. X. Gao, Y. Sha, Q. Lin, R. Cai, M. O. Tade, and Z. Shao, *J. Power Sources* 275 (2015) 38-44.
5. G.-H. An, D.-Y. Lee, and H.-J. Ahn, *ACS Appl. Mater. Interfaces* 8 (2016) 19466-19474.
6. Q. Zhang, J.-J. Chen, X.-Y. Wang, C. Yang, M.-S. Zheng, and Q.-F. Dong, *Phys. Chem. Chem. Phys.* 17 (2015) 10353-10357.
7. C. H. Jiang, S. X. Dou, H. K. Liu, M. Ichihara, and H. S. Zhou, *J. Power Sources* 172 (2007) 410-415.
8. Y. Chen, K. Xie, Y. Pan, and C. Zheng, *J. Power Sources* 196 (2011) 6493-6497.
9. K. R. Ragavendran, H. Xia, G. Yang, D. Vasudevan, B. Emmanuel, D. Sherwood, and A. K. Arof, *Phys. Chem. Chem. Phys.* 16 (2014) 2553-2560.
10. I.-M. Hung, Y.-C. Yang, H.-J. Su, and J. Zhang, *Ceram. Int.* 41 (2015) S779-S786.
11. B.-R. Koo, S.-T. Oh, and H.-J. Ahn, *Mater. Lett.* 178 (2016) 288-291.
12. G.-H. An, B.-R. Koo, and H.-J. Ahn, *Phys. Chem. Chem. Phys.* 18 (2016) 6587-6594.

13. K. M. Shaju and P. G. Bruce, *Chem. Mater.* 20 (2008) 5557-5562.
14. D. Guo, X. Wei, Z. Chang, H. Tang, B. Li, E. Shangguan, K. Chang, X.-Z. Yuan, and H. Wang, *J. Alloys. Compd.* 632 (2015) 222-228.
15. K. Saeed, S. Haider, T.-J. Oh, and S.-Y. Park, *J. Membr. Sci.* 322 (2008) 400-405.
16. O. Toprakci, H. A. K. Toprakci, L. Ji, G. Xu, Z. Lin, and X. Zhang, *ACS Appl. Mater. Interfaces* 4 (2012) 1273-1280.
17. Y.-P. Fu, Y.-H. Su, C.-H. Lin, and S.-H. Wu, *Ceram. Int.* 35 (2009) 3463-3468.
18. T. Cui, N. Hua, Y. Han, and X. Kang, *Inorg. Mater.* 44 (2008) 542-548.
19. K. W. Kim, M. R. Kim, S.-W. Lee, K.-S. Han, and S. I. Woo, *Chem. Vap. Depos.* 9 (2003) 187-192.
20. C. V. Ramana, M. Massot, and C. M. Julien, *Surf. Interface Anal.* 37 (2005) 412-416.
21. N. Treuil, C. Labrugère, M. Menetrier, J. Portier, G. Campet, A. Deshayes, J.-C. Frison, S.-J. Hwang, S.-W. Song, and J.-H. Choy, *J. Phys. Chem. B* 103 (1999) 2100-2106.
22. G. An, P. Yu, M. Xiao, Z. Liu, Z. Miao, K. Ding, and L. Mao, *Nanotechnology* 19 (2008) 275709.
23. Y.-L. Ding, X.-B. Zhao, J. Xie, G.-S. Cao, T.-J. Zhu, H.-M. Yu, and C.-Y. Sun, *J. Mater. Chem.* 21 (2011) 9475-9479.
24. F.-Y. Shih and K.-Z. Fung, *J. Power Sources* 159 (2006) 179-185.
25. A. Subramania, N. Angayarkanni, and T. Vasudevan, *Mater. Chem. Phys.* 102 (2007) 19-23.
26. H. M. Wu, J. P. Tu, Y. F. Yuan, X. T. Chen, J. Y. Xiang, X. B. Zhao, and G. S. Cao, *J. Power Sources* 161 (2006) 1260-1263.
27. X. Li, R. Xiang, T. Su, and Y. Qian, *Mater. Lett.* 61 (2007) 3597-3600.
28. Y. Meng, X. Liu, L. Liu, B. Li, X. Zhao, L. Feng, Y. Wang, and W. Wang, *Chem. Res. Chin. Univ.* 31 (2015) 820-824.
29. F. Cheng, H. Wang, Z. Zhu, Y. Wang, T. Zhang, Z. Tao, and J. Chen, *Energy Environ. Sci.* 4 (2011) 3668-3675.
30. J. Wang, Q. Zhang, X. Li, Z. Wang, H. Guo, D. Xu, and K. Zhang, *Phys. Chem. Chem. Phys.* 16 (2014) 16021-16029.